Journal of
Applied Physics

RESEARCH ARTICLE | AUGUST 28 2026

Theoretical model of microparticle-assisted super-resolution microscopy

A. R. Bekirov; N. A. Lystseva; N. V. Grednev; B. S. Luk'yanchuk; A. A. Fedyanin

J. Appl. Phys. 140, 083104 (2026)
https://doi.org/10.1063/5.0340761

Journal of
Applied Physics

ARTICLE

pubs.aip.org/aip/jap

Theoretical model of microparticle-assisted super-resolution microscopy

Cite as: J. Appl. Phys. **140**, 083104 (2026); doi: 10.1063/5.0340761
Submitted: 27 April 2026 · Accepted: 9 August 2026 ·
Published Online: 28 August 2026

View Online Export Citation CrossMark

A. R. Bekirov,[a)] N. A. Lystseva, N. V. Grednev, B. S. Luk'yanchuk, and A. A. Fedyanin

AFFILIATIONS

Faculty of Physics, Lomonosov Moscow State University, Moscow 119991, Russia

[a)] **Author to whom correspondence should be addressed:** bekirovar@my.msu.ru

ABSTRACT

We present the three-dimensional theoretical model of microparticle-assisted super-resolution imaging that enables simulation of virtual image formation. The model shows that partial spatial coherence of the illumination is a key prerequisite for achieving super-resolution. We demonstrate that a spherical microparticle enhances the resolving power of an optical system with a limited numerical aperture, allowing features near the particle to be resolved up to the Abbe limit. To overcome this limit, high-frequency oscillations in the spatial correlation function of the radiation are required, leading to out-of-phase superposition of image contributions from different object points. We further show that, in this regime, the optical resolution deteriorates as the object size decreases. Overall, the results establish a consistent framework that reproduces experimentally observed subwavelength imaging and clarifies the underlying physical mechanisms.

INTRODUCTION

In 2011, a super-resolution imaging effect using dielectric microparticles was discovered,[1] whereby placing a transparent microparticle of a few microns in diameter onto the sample enables the visualization of fine details that are unresolvable under conventional microscopy. This phenomenon is observed in the magnified virtual image produced by the microparticle. Since then, the technique has rapidly evolved, with efforts focused on improving image quality and controlling particle positioning for the visualization of extended structures. Recent experimental demonstrations have shown that combining microsphere-assisted microscopy with evanescent wave illumination enables the imaging of low-contrast objects.[2] This technique offers significant potential for the high-resolution study of biological specimens, a field where non-invasive methods are of paramount importance. A comprehensive review of theoretical and experimental studies can be found in Ref. 3.

Despite growing research interest, there is still no widely accepted theoretical model for this effect. Such a model is required to clarify the physical origin of the effect and to enable predictive optimization of imaging performance under different illumination and sample conditions. Many prior studies attempted to simulate radiation propagation and image formation in the presence of a microparticle, but due to computational complexity, most models were limited to two-dimensional configurations.[4–6] However, 2D models fail to capture the geometry of realistic samples—such as nanodisk arrays or patterned surfaces—which makes a quantitative comparison with experimental data difficult, despite its importance for model validation.

In this work, we propose a full three-dimensional model for microparticle-assisted super-resolution imaging. The model accounts for the spatial coherence of illumination, broadband and narrowband spectra, and different illumination geometries. We validate the results against several experimental datasets. While a spherical microparticle is used in the simulations, the approach can be extended to other particle shapes.

Methods

Image field formation algorithm

Let a spatially coherent incident field $\mathbf{E}_{inc}$ illuminate a given system at frequency ω. The temporal dependence is assumed to take the form $\sim e^{-i\omega t}$. As a result of diffraction, a new field distribution $\mathbf{E}$ is formed in the surrounding space. We assume that the field $\mathbf{E}$ is observed by an ideal aberration-free optical system with 1:1 magnification, located at infinity, in the half-space $z > 0$ (see Fig. 1). The resulting image field $\mathbf{E}_{im}$ can be computed by applying the diffraction integral to the complex conjugate field via the

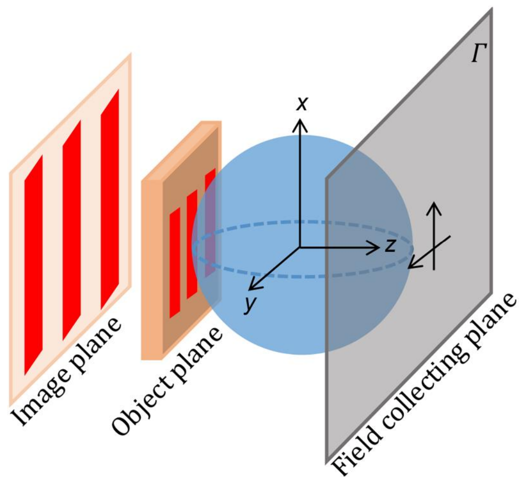

FIG. 1. General simulation scheme for imaging objects in the virtual image formed by a microparticle. The image is calculated as a time-reversed wave with respect to plane Γ. The resulting virtual image is located below the contact point between the microparticle and the sample.

following expression:[7]

$$\mathbf{E}_{im} = \iint\limits_{\Gamma} \left(\frac{i\mu_0}{n_0}([\mathrm{n}, \mathbf{H}^*]G + ([\mathrm{n}, \mathbf{H}^*], \nabla)\nabla G) - [[\mathrm{n}, \mathbf{E}^*], \nabla G] \right) \frac{k^2 dS}{4\pi}, \tag{1}$$

where $G = \exp(ik|r - r_0|)/k|r - r_0|$, $\nabla = k^{-1}\partial/\partial \boldsymbol{r}_0$, $k = 2\pi/\lambda$, and Γ is the surface homotopic to the plane, μ_0 and n_0 represent the magnetic permeability and the refractive index of the surrounding medium, respectively. In our calculations, we assumed $\mu_0 = n_0 = 1$. By applying Eq. (1) to the complex conjugates of the fields **E** and **H**, the evanescent components are suppressed, and the outgoing wave transforms into a converging one, which corresponds to a time-reversed wave.[8] To compute the image produced by an incoherent source, the image field must be intensity-averaged over different realizations of the incident fields $\mathbf{E}_{inc}$. Additionally, if the source has a broadband spectrum, averaging over frequency is also required, so that

$$I_{im}^{non.\ coh}(r) = \frac{c}{8\pi} \iint |\mathbf{E}_{im}(r, \omega, \mathbf{E}_{inc})|^2 dE_{inc} d\omega. \tag{2}$$

The differential element dE_{inc} parameterizes the geometry of the incident illumination. The specific form of the field $\mathbf{E}_{inc}$ depends on the illumination conditions of the system. In the most commonly used Köhler illumination scheme, the incident field is given by $\mathbf{E}_{inc} = \mathbf{E}_0 \exp(i\mathbf{k}\cdot\mathbf{r})$, with $dE_{inc} = dk_x dk_y$, i.e., the sample is illuminated by plane waves coming from different angles. In the case of critical illumination, the incident field is a focused Gaussian beam. The general calculation scheme is illustrated in Fig. 1, where the microsphere is placed in direct contact with the sample under investigation.

Diffraction field models for the microsphere

To implement the described algorithm, it is necessary to determine the electric and magnetic fields **E** and **H** on the specified surface Γ above the microsphere (see Fig. 1). In this work, we employed two approaches for calculating these fields. The first approach, referred to as the Full Model (FM), involves a complete simulation of the electromagnetic field in the volume surrounding the microsphere. The second approach, termed the Simple Model (SM), considers only the field propagation in the vicinity of the contact region between the microsphere and the sample, which significantly reduces the computational domain.

Full model simulation

The simulation of the fields **E**, **H** was carried out using FDTD algorithm on a standard square computational grid with a spatial step size of $dx = dy = dz = 0.027\,\mu$m. In the vicinity of the structures under consideration, the spatial grid was locally refined in order to accurately resolve the geometrical features of the objects. The time step was determined automatically by the Lumerical FDTD solver according to the standard Courant stability criterion. The simulation domain was $9 \times 9 \times 6.8\,\mu\mathrm{m}^3$. The lateral size of the surface Γ sets the maximum collection angles from the sample, defining the effective objective numerical aperture NA. In the present model, NA ≈ 0.7. All materials are considered non-dispersive with a constant refractive index; the microsphere had a diameter of $5\,\mu$m. Figure 1 shows the general layout of the simulation. Standard built-in sources from the Lumerical FDTD package were used to generate plane wave and Gaussian beam excitations. The field $\mathbf{E}_0$ was assumed to be polarized either as a TM or TE wave with respect to the substrate surface. The surface Γ was implemented as a monitor placed directly above the microsphere, performing spectral Fourier transforms for a given set of frequencies. This provided the field components $\mathbf{E}(x, y, \omega_i)$ and $\mathbf{H}(x, y, \omega_i)$ that were then used in Eq. (1).

Simple model simulation

In the SM, the fields **E** and **H** are simulated only in the contact region between the microsphere and the sample. Knowing the fields in the sample plane, the subsequent propagation of light through the microsphere can be analytically calculated using the Huygens–Fresnel principle in combination with Mie theory. This approach neglects the secondary illumination of the sample by the waves circulating inside the microsphere, which may have a significant impact under resonant conditions.

The specification of the source field in the SM varies with the visualization geometry. In the reflection mode, the microsphere affects the illumination field, since the radiation first passes through the microsphere and then reaches the sample. To account for this effect, we applied Mie theory for a sphere in free space to calculate the diffraction of the incident field on the microsphere and used the resulting near field distribution as the source field. Note that the field distribution within a particle placed on a substrate deviates from that in free space due to the interference of waves reflected at the boundaries. The contribution of these effects may become significant in the vicinity of resonances and can potentially lead to qualitative differences between the SM and FM descriptions. Nevertheless, for the non-resonant configurations examined in this work, their impact appears to be predominantly quantitative, resulting mainly in variations in the image amplitude, while no qualitative changes in the image formation were observed. In the transmission mode, where the illumination first passes through the sample and then through the microsphere, the source field can be defined in the same way as in the Full Model, without any modification of the incident wavefront. See the supplementary material for details of the SM algorithm.

Comparison of the models

Figure 2 shows a comparison of the simulation domains in the two models, as well as the positions of the field monitors and the source regions within the computational volume. In the SM, the fields on the surface Γ are calculated using the Huygens–Fresnel principle applied to the fields defined on the auxiliary surface Γ_{near} [see Figs. 2(c) and 2(d)].

Two circular apertures with diameters of 250 nm were considered as test objects. The apertures were patterned in a perfectly conducting film of 10 nm thickness, with a center-to-center separation of 300 nm. The illumination wavelength was 500 nm. In the reflection mode, the structure was complementary to the transmissive one, with identical geometric parameters. The illumination was arranged in a Köhler configuration with a cone angle of π/4, corresponding to an illumination numerical aperture of $NA_{ill} = \sin(\pi/4) \approx 0.7$. Under these conditions, the two objects are unresolved in direct imaging [see Figs. 3(a) and 3(d)]. However, when viewed through the microsphere, the objects become distinguishable, as confirmed by both models in the transmission mode [Figs. 3(b) and 3(c)] and in the reflection mode [Figs. 3(e) and 3(f)].

For the Simple Model, the simulation domain has approximate dimensions of $4 \times 4 \times 1.5\,\mu m^3$, whereas the Full Model employs a computational volume of $10 \times 10 \times 7\,\mu m^3$, respectively. Due to the smaller numerical domain, simulations using the SM run roughly 100 times faster than those with the FM. See the supplementary material for details.

RESULTS

Full model result

Broadband source with Köhler illumination scheme

To validate our model, we begin by simulating the imaging of a Blu-ray disk surface, a benchmark structure that has been widely studied in experimental works.[1,9] The disk was modeled as a multilayer structure consisting of the following elements: an infinite glass substrate (refractive index $n = 1.46$), a 30 nm thick metal layer (with refractive index $n = 0.77 + i6.08$), and a patterned surface composed of parallel trenches 200 nm wide, separated by 100 nm gaps and 30 nm deep, with the same refractive index as the metal layer. Let us consider the geometry proposed in the experimental work:[9] barium titanate glass (BTG) microspheres with a refractive index of $n = 1.95$ were immersed in an immersion liquid (water, $n = 1.33$).

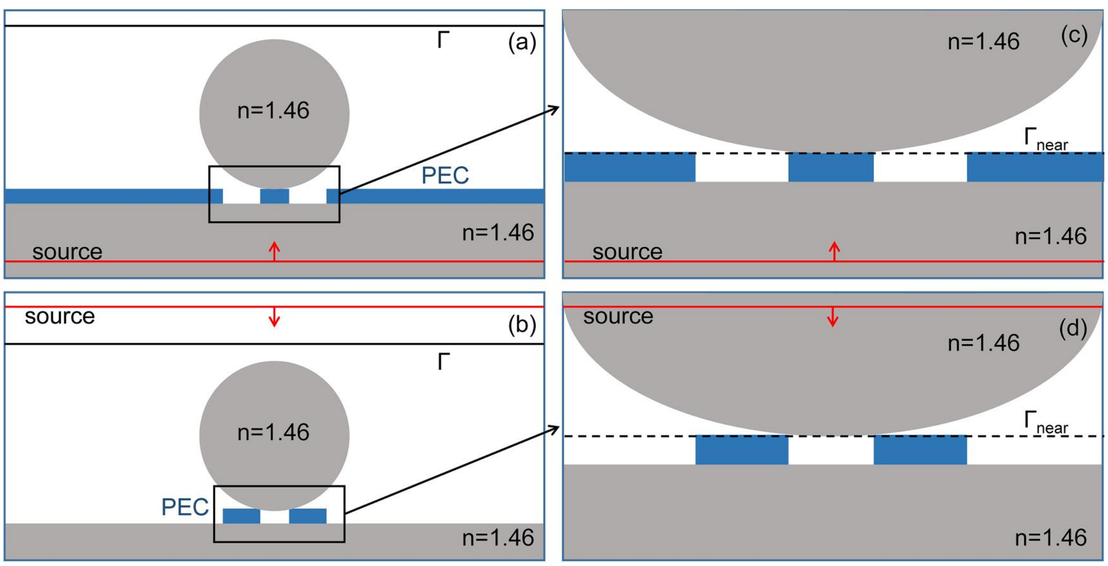

FIG. 2. Comparison of the simulation domains (not to scale) for the FM and SM. (a–b) Side views of the FM in the reflection and transmission modes, respectively. (c–d) Corresponding configurations for the SM. In panel (d), the source field is defined with the wavefront distortion induced by the microsphere taken into account. The positions of the field monitors coincide with the surfaces Γ. The microsphere radius is 2.5 μm. The computational domain boundaries are enclosed by perfectly matched layers (PML).

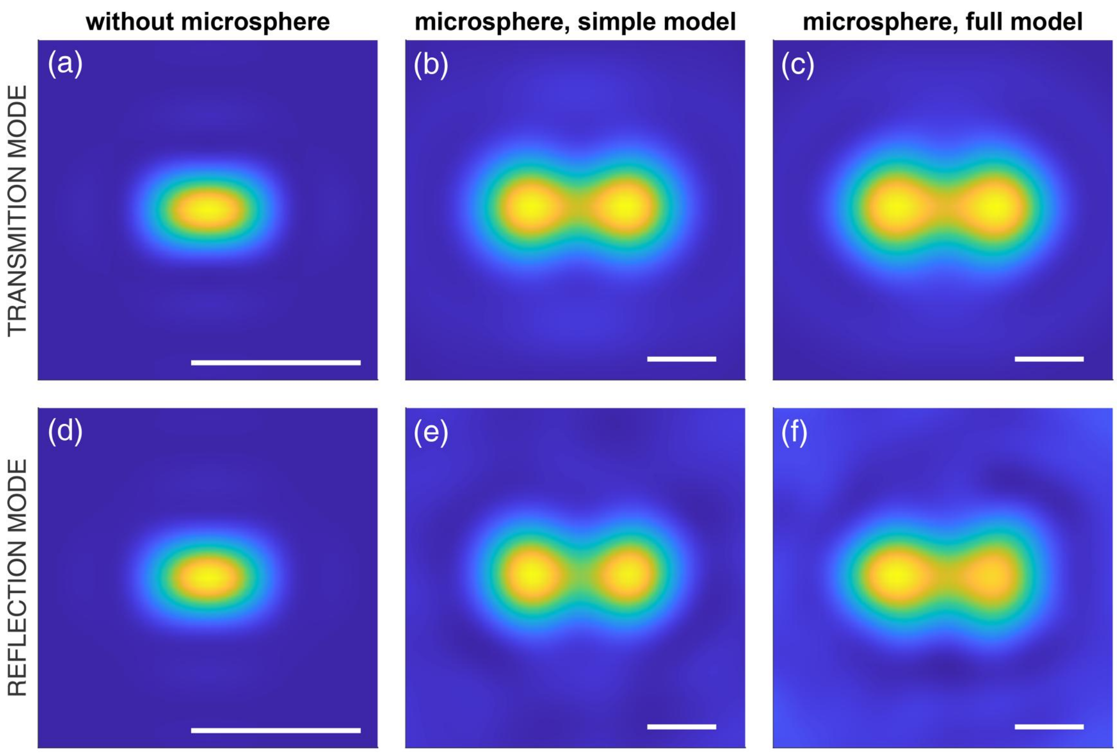

FIG. 3. Comparison of the FM and SM for the formation of the virtual image by a microsphere. Images of two nanoscale apertures with a diameter of 250 nm and edge-to-edge separation of 50 nm in a perfectly conducting film in reflection mode: (a) without the microsphere, (b) with the microsphere using the SM, and (c) using the FM. Panels (d–f) show the corresponding comparison for two disks in reflection mode. In free space, the image plane coincides with the object plane. When the microsphere is present, the image is observed in the plane $z/R = -5$ relative to the center of the microsphere. Scale bar: 1 μm. Ratio of peak intensities: (b)–(c) 1:1.07; (e)–(f) 1.15:1.

The simulation results are shown in Fig. 4. Similar to Ref. 9, a strong dependence of the observed pattern on the polarization of the recorded image is observed. To simulate the image at different polarizer orientations, the calculation of the image intensity (2) included only the x- or y-component of the field $\mathbf{E}_{im}$ (1).

The illumination cone had an angular aperture of $\pi/9$, and included 50 uniformly distributed plane wave directions. The source spectrum had a peak at $\lambda = 500$ nm and spanned wavelengths from 400 to 700 nm (for more details, see the supplementary material). The illumination geometry was manually adjusted to achieve the best agreement between the simulated and experimental results reported in Ref. 9. A strong dependence of the image contrast and pattern on the illumination geometry was observed.

Monochromatic source at 405 nm with critical illumination

Among the most notable achievements of microsphere-assisted imaging is its integration with confocal microscopy, which has demonstrated record-breaking resolution of nanostructures. In particular, nanodisks with diameters of 135 nm spaced only 25 nm apart were successfully resolved.[10]

Unlike conventional microscopes operating under Köhler illumination, a confocal microscope uses a focused beam to illuminate each point of the sample individually. The image is formed by scanning the region of interest and reconstructing the complete image from individual focus points. Therefore, to model image formation in a confocal microscope, it is necessary to use a focused beam rather than plane waves.

In our simulations, we assumed that the source is focused on the sample surface, thereby implementing the classical critical illumination scheme. The illumination cone had an angular aperture of $\pi/4$ and consisted of 103 uniformly distributed wave directions. It is worth noting that achieving super-resolution in this configuration requires a sufficiently wide illumination cone. The disks were positioned on a transparent substrate ($n = 1.46$), coaxially aligned with the center of the microparticle.

In order to achieve optimal image contrast under the given illumination conditions, it is essential to suppress radiation propagating close to the surface normal. To this end, the signal amplitude of rays focused within the illumination cone at angles $\theta < \pi/12$ was attenuated by a factor of 10. In practice, this requirement is readily fulfilled by blocking the light originating from the central part of the source. This step is crucial to avoid dominance of the

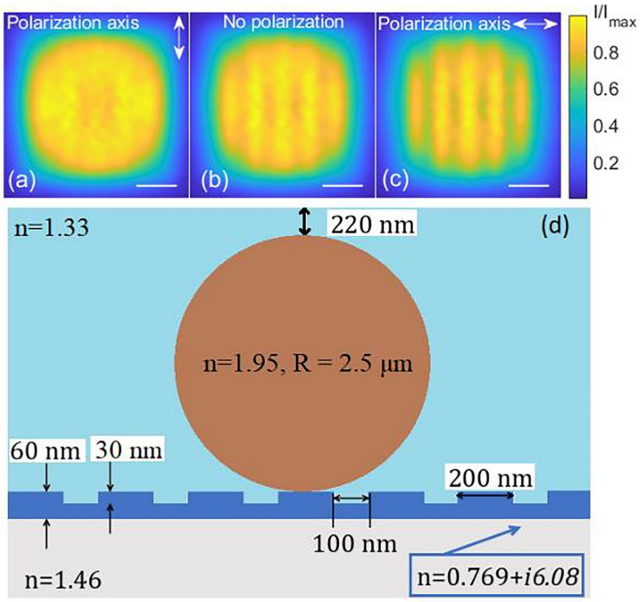

FIG. 4. Virtual images of the Blu-ray disk surface obtained at different polarizer orientations (Compare with Fig. 4 in Ref. 9). The observation plane is located at a depth of $z = -6.25\,\mu$m below the substrate surface. The relative intensities of the maxima in (a)–(c) are 1:1.8:1.1, respectively. Scale bar: 2.5 μm. (d) Schematic view of the considered geometry. The immersion liquid, water ($n = 1.33$), barely covers the microparticle placed on the surface of the Blu-ray disk.

central lobe, which would, otherwise, obscure finer image details. The results are presented in Fig. 5, which displays images of the nanodisks under two illumination conditions. We also applied our model to simulate an array of perfectly conducting dimers with 120 nm width and 60 nm spacing, as described in Ref. 11. In this case, the structure is successfully visualized using our approach (see the supplementary material).

These examples enable a fundamental study of the resolving power of a microsphere and the key factors underlying its super-resolution. In our earlier work,[12] based on a two-dimensional numerical model, we showed that as the size of the objects imaged through a microsphere decreases, the resolution approaches the classical Abbe limit of λ/2. To extend this hypothesis to three dimensions, we modeled each nanodisk as a point-like incoherent source placed at its center. The simulations demonstrate that such sources are indistinguishable. A similar calculation, with the sources located on the nanodisk surfaces, yielded the same result: the structures remained unresolved. Although the disks retain their characteristic size, each of them emits independently. These findings highlight a fundamental requirement for super-resolution: spatial coherence of illumination.

The presence of partial spatial coherence effects in the illumination indicates that the simulation results strongly depend on the specific field distribution in the region of the disks. The substrate material can also influence this distribution, as noted in Ref. 13. Our model shows that if a similar calculation is performed without accounting for the substrate, i.e., considering the disks in free space with the microparticle above them, the structure becomes indistinguishable, even accounting for the spatial coherence of the illumination.

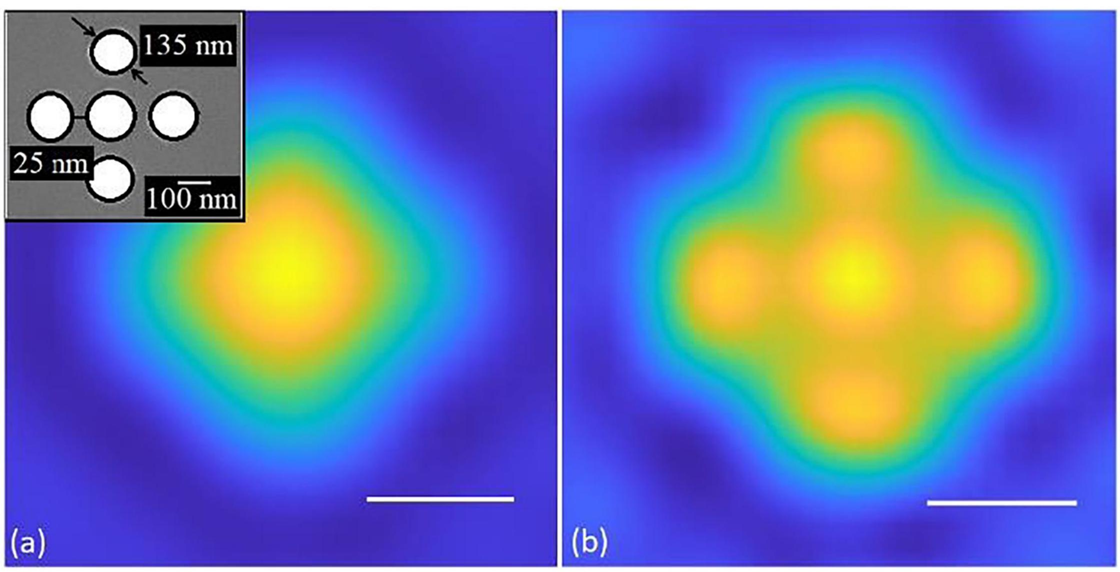

FIG. 5. (a) Virtual image of five nanodisks with the geometry shown in the inset, obtained under critical illumination. (b) Corresponding image with the illumination suppressed inside the cone $\theta < \pi/12$. Both images are taken in the observation plane at $z = -10\,\mu$m below the substrate surface. Scale bar: 1 μm.

Simple model result

The FM enables the investigation of a wide range of problems related to microsphere-based imaging; however, this approach requires significant computational efforts. For a fixed system geometry, the FM may be appropriate, but when exploring the influence of variations in geometry or illumination, the computations become prohibitively complex. For this reason, in the present work, we employ simulations according to the SM with the Köhler illumination scheme at a wavelength of $\lambda = 500$ nm.

Influence of spatial coherence effects

As shown for nanodimers, partial-coherence effects in microsphere-based imaging enhance resolution. Here, we consider off-axis annular or dark-field illumination to increase the coherence of the radiation. This illumination scheme enhances the resolving power of a microparticle, a concept first introduced in Ref. 14 for a two-dimensional model. Figure 6 presents transmission-mode images of an array of nine apertures in an ideal conductor, each with a diameter of 180 nm and a period of 200 nm, obtained for various illumination geometries. The structure is placed on a substrate with a refractive index $n_{sub} = 1.46$, as shown in Fig. 2. The imaging plane is located at $z/R = -5$ with respect to the center of the microparticle. The simulations indicate that the virtual image forms near the geometrical focus at $z/R \approx -3$ and improves upon further downward shift of the imaging plane, while excessive displacement leads to image degradation.

In this example, the distance between adjacent apertures is below the diffraction limit. Under conventional Köhler illumination, the structure cannot be resolved by the microparticle [Fig. 6(a)]. Suppression of the low spatial-frequency components of the source modifies the spatial correlation function of the incident field by introducing oscillations, thereby improving the resolution [Figs. 6(b) and 6(c)]. The peak intensity amplitudes in Figs. 6(a) and 6(c) are in the ratio 24.8:7.4:1.9. After normalization of the incident field by the number of plane-wave components used in the calculation, the corresponding ratio becomes 8.2:3.2:1.6.

The enhancement of the resolving capability of the microparticle under annular illumination is observed for structures whose characteristic dimensions are comparable to the illumination wavelength. When the diameter of the nanoapertures is reduced to 40 nm (λ/12.5) while keeping the center-to-center separation unchanged, the structure becomes unresolvable (see the supplementary material). Partial coherence effects may also influence the resolution in free space; however, this structure remains unresolvable for all considered illumination schemes, even when the objective numerical aperture reaches $NA_{obj} = 1$ (see the supplementary material).

The normalized correlation function 15 of the radiation is defined as

$$\gamma(\mathbf{r},\boldsymbol{\rho}) = \frac{\langle(\mathbf{E}(\mathbf{r}),\mathbf{E}^*(\mathbf{r}+\boldsymbol{\rho}))\rangle_t}{\sqrt{\langle|\mathbf{E}(\mathbf{r})|^2\rangle\langle|\mathbf{E}(\mathbf{r}+\boldsymbol{\rho})|^2\rangle}}.$$

Under annular illumination, the correlation function of the incident field can be calculated as follows:

$$\gamma^{inc}(\rho) = 2\left(NA_{outer}^2 - NA_{inner}^2\right)^{-1}\int_{NA_{inner}}^{NA_{outer}} xJ_0(n_{sub}k\rho x)dx,$$

where NA_{inner} and NA_{outer} specify the lower and upper limits of the transverse wave vectors. Interaction with the structure modifies the field distribution and, consequently, the correlation function, i.e., $\gamma \neq \gamma^{inc}$. Under annular illumination, γ^{inc} exhibits pronounced oscillations, causing the near-field correlation function γ to change sign between adjacent apertures (see Fig. 6). As a result, the fields scattered by neighboring nanoapertures interfere out of phase, leading to enhanced resolution. The image fields produced by individual apertures partially overlap. When combined in phase, they merge into a single broad maximum [Fig. 6(a)]. In contrast, out-of-phase superposition suppresses the overlapping intensity contributions through partial cancellation, resulting in the appearance of nine distinct maxima [Figs. 6(b) and 6(c)]. This effect is illustrated in Fig. 7 using the example of two exponential functions.

The resolution enhancement provided by the microparticle, compared to free space, originates from the modification of the point spread function. By analogy with Fig. 7, the microparticle reshapes the fields E_1 and E_2 making their superposition with the appropriate relative phase becomes resolvable, whereas the same superposition of the unmodified fields remains unresolved.

This statement can be verified analytically using a model of point sources, without resorting to numerical simulations. Let us consider an array of N point dipoles with partially correlated random phases φ_j. The total electromagnetic field generated by the system is described by

$$\Delta\mathbf{E} + k^2\mathbf{E} = -4\pi k^{-1}\sum\nolimits_{j=1}^{N} e^{i\varphi_j}\delta(\mathbf{r}-\mathbf{r}_j)\mathbf{e}_x,$$

where the statistical properties of the phases are governed by the correlation function,

$$\left\langle e^{i(\varphi_m-\varphi_m)}\right\rangle = \gamma(|\mathbf{r}_m - \mathbf{r}_n|).$$

The total intensity of the virtual image is expressed in terms of the individual image fields $\boldsymbol{E}_{im}{}^{(j)}$ as

$$I_{im} = \frac{c}{8\pi}\langle|\mathbf{E}_{im}|^2\rangle \sim \sum\nolimits_{i,j=1}^{N}\left(\mathbf{E}_{im}^{(i)},\mathbf{E}_{im}^{(j)*}\right)\gamma(|\mathbf{r}_m - \mathbf{r}_n|).$$

The presence of the microparticle modifies the image fields $\boldsymbol{E}_{im}{}^{(j)}$ but does not alter the form of the correlation function γ. The fields $\boldsymbol{E}_{im}{}^{(j)}$ are obtained analytically from Mie theory and Eq. (1). Three forms of the second-order correlation function γ are analyzed: (i) fully incoherent dipoles, (ii) partially coherent dipoles with a correlation function corresponding to Köhler illumination with $\mathrm{NA}_{ill} = 1$, and (iii) annular illumination with $\mathrm{NA}_{inner} = \mathrm{NA}_{outer} = 1$, corresponding to ring illumination with $k_z = 0$. The corresponding correlation functions are given by

$$\gamma(\rho) = \begin{cases} \delta(k\rho) \\ 2J_1(k\rho)/(k\rho), \\ J_0(k\rho) \end{cases}$$

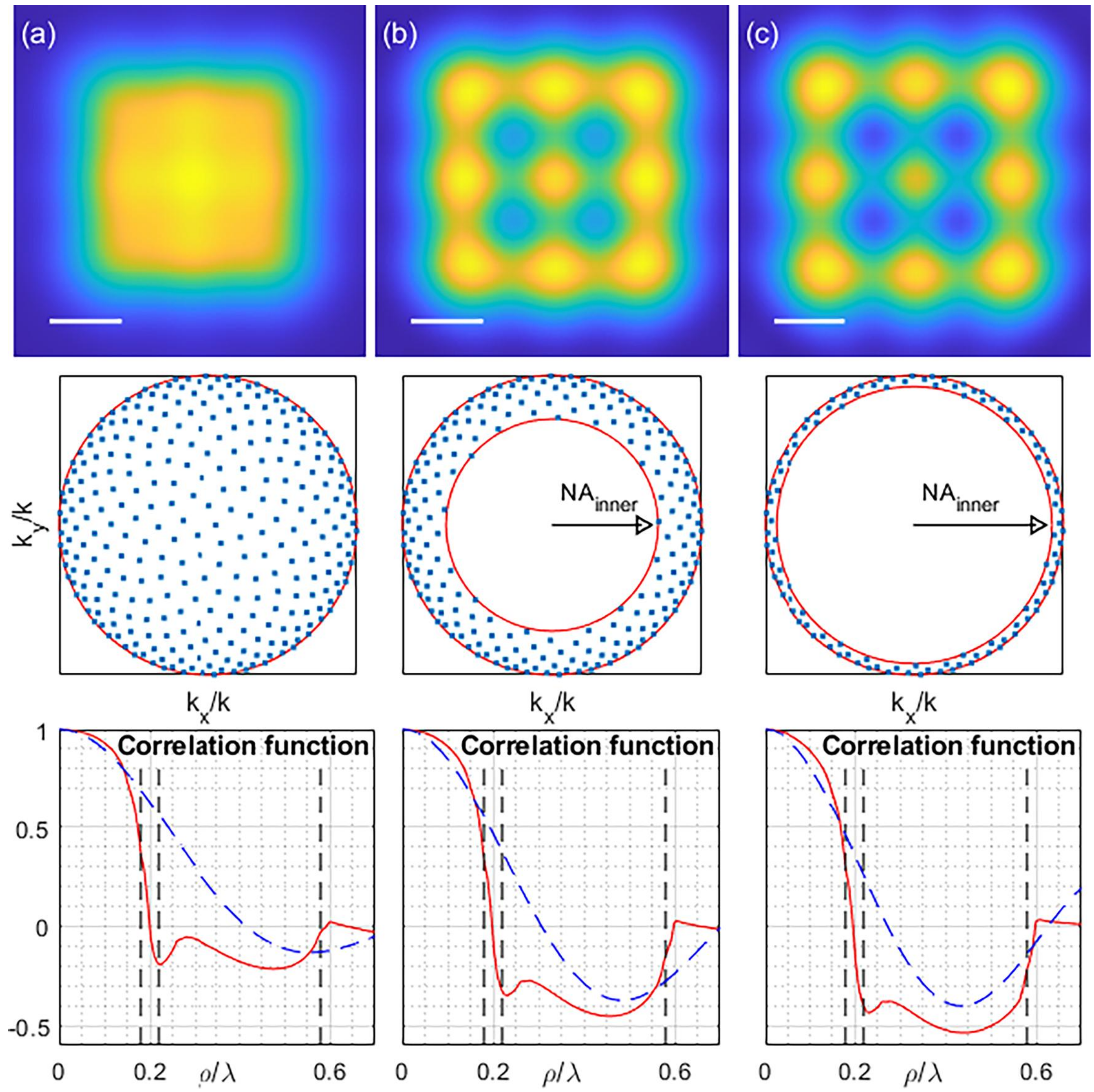

FIG. 6. Image field of an array of nine nanoapertures (diameter 180 nm, period 200 nm, λ = 500) in an ideally conducting film for different NA_{inner}: (a–c) 0, 0.7, and 0.92, respectively. The illumination directions used in the simulations are shown at the bottom of each panel, along with the corresponding correlation functions of the incident radiation γ^{inc} (blue dashed line) and near field γ (red line). The variation in the function γ is shown between the central and adjacent nanoapertures, where vertical dashed lines indicate the boundaries of the nanoholes. The observation plane is located at z/R = − 5. Scale bar: 1 μm.

where δ is the Kronecker delta and J denotes the Bessel function of the first kind.

The source array consists of two square regions of size $w = \lambda/3$, separated by a distance $d = 0.185\lambda$, located in the plane $z = -R$ and arranged symmetrically with respect to the center of the microsphere. The virtual image is observed through an objective with numerical aperture $NA_{obj} = 0.9$.

Figure 8 shows the resulting virtual images in free space and in the presence of a microsphere ($n = 1.46$, $2\pi R/\lambda = 30$) for different forms of γ. The comparison reveals a pronounced dependence of the microsphere-induced resolution enhancement on the shape of the correlation function.

For sufficiently large separations d, similar coherence-induced effects can also be observed in free space. Therefore, the microsphere primarily amplifies the influence of partial coherence on the resolving capability. In the considered example, the effects of partial coherence are induced by the external illumination field; therefore, similar effects are observed both in the presence of a microparticle and in free space. However, in reflection-mode imaging, the presence of a microparticle can strongly modify the

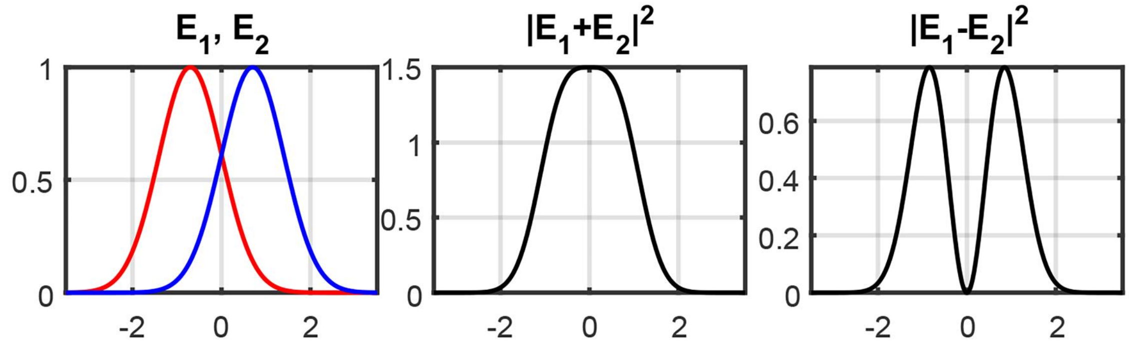

FIG. 7. The resulting virtual image is located below the contact point between the microparticle and the sample. Comparison of the sum and difference of two laterally shifted Gaussian functions, $E_1 = exp[-(x - 0.7)^2]$ and $E_2 = exp[-(x + 0.7)^2]$.

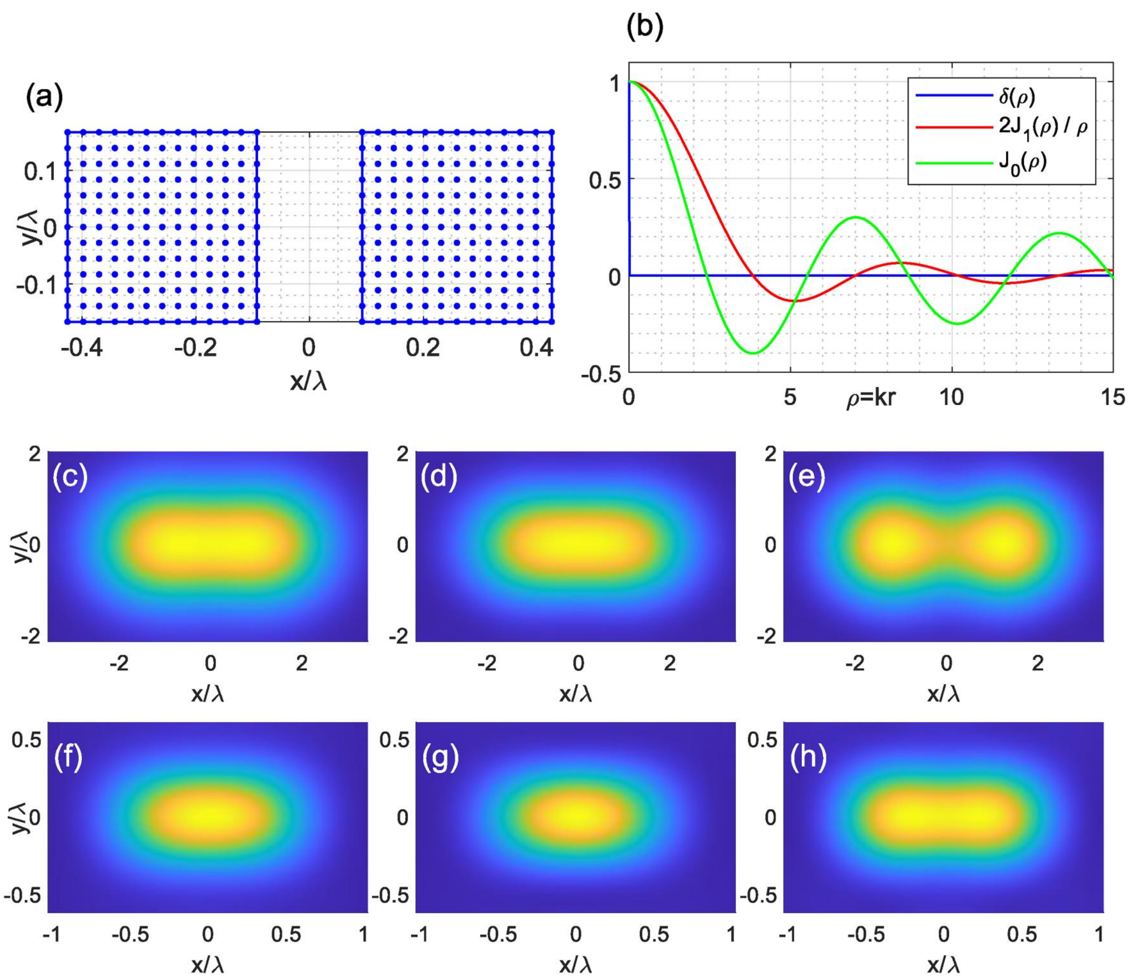

FIG. 8. (a) Point-sources geometry. (b) Correlation functions used in the calculations. (c–e) Virtual images of the dipole array formed by the microparticle ($n = 1.46$, $2\pi R/\lambda = 30$) in the plane $z/R = -4.5$ using $\gamma = \delta(\rho)$, $2J_1(\rho)/\rho$, $J_0(\rho)$, respectively. (f–h) Corresponding free-space images; the image plane coincides with the source plane.

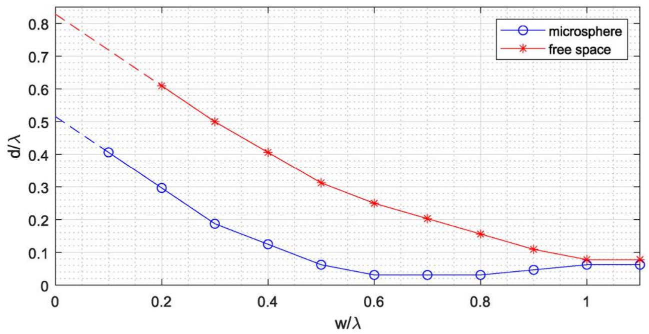

FIG. 9. The minimum edge-to-edge separation as a function of the nanohole diameter w under Köhler illumination ($NA_{ill} \approx 0.92$, $NA_{obj} \approx 0.72$) for microsphere-assisted imaging and free-space imaging. The dashed lines indicate extrapolated behavior in the limit of vanishing nanohole diameter, where direct numerical calculations become impractical due to the required refinement of the computational grid near the apertures.

field distribution illuminating the sample, giving rise to effects that are fundamentally absent in free space.

An illustrative example is the critical illumination regime shown in Fig. 5. In this case, the microsphere effectively "mixes" radiation incident over its entire surface and refocuses it onto the nanodisks, whereas in free space, the nanodisks reflect only the portion of the field that is locally focused in their vicinity. Another example is secondary illumination of the sample. Acting as an optical resonator, the microsphere can store electromagnetic energy, leading to a secondary illumination effect,[4] which, under resonant conditions, can further enhance the resolving power of the microparticle.[12]

Resolution analysis

In this section, we examine the resolution limit of the microsphere as the size of the investigated objects is progressively reduced. We consider standard Köhler illumination in the transmission configuration, as well as the case where the central part of the illumination within the inner numerical aperture, NA_{inner}, is blocked [Figs. 6(b) and 6(c)]. The test objects are identical to those shown in Fig. 3(b) and consist of two disks patterned in a perfectly conducting film on a dielectric substrate. The image plane is located at $z/R = -5$ relative to the center of the microsphere. The surface Γ is defined as a square region of size 4Rx4R at $z/R = 1.1$, which corresponds to an objective numerical aperture of $NA_{obj} \approx 0.72$. The illumination numerical aperture is chosen as $NA_{ill} = \sin(3^*\mathrm{pi}/8)$. Note that, since the rays transmitted through the microparticle are confined within a limited divergence cone, increasing the size of plane Γ—and thus, the objective numerical aperture NA_{obj}—results in only minor modifications of the image formed by the microparticle. This trend is consistent with the experimental observations reported in Ref. 16.

The minimum edge-to-edge separation (d) between the structures is determined from the condition that the valley intensity between adjacent maxima reaches approximately 80% of the peak intensity, corresponding to the classical Rayleigh criterion, where the maximum of one Airy disk coincides with the first minimum of the other. The resolution was determined with an accuracy of λ/50 using the same algorithm as described in Ref. 12. Figure 9 shows the dependence of the optical resolution on the structure

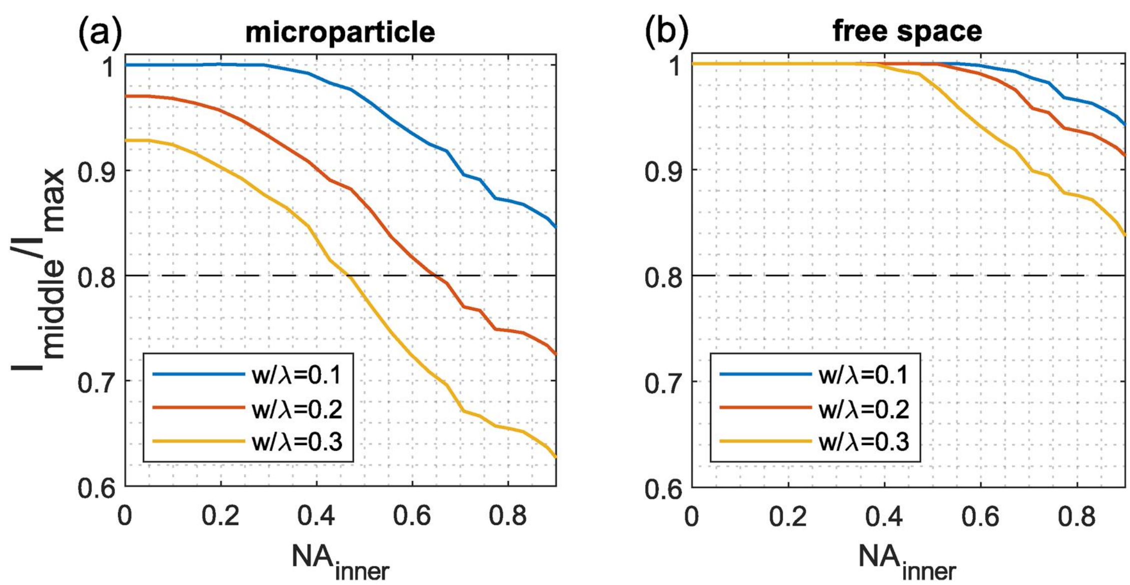

FIG. 10. Image contrast $C = I_{middle}/I_{max}$ for nanoholes of different diameters w at a fixed center-to-center separation of 0.4λ as a function of the inner numerical aperture NA_{inner}: (a) microsphere-assisted imaging and (b) free-space imaging. As seen in (a), increasing the nanohole diameter w leads to higher image contrast and enhanced resolving capability.

diameter. Based on these calculations and in agreement with the two-dimensional model,[12] the resolution limit of the microparticle under Köhler illumination can be expressed as the following criterion:

$$d + w \approx \frac{\lambda}{2}, \tag{3}$$

where w is the characteristic object size (nanohole diameter) and d is the minimum edge-to-edge separation. Equation (3) holds for $w < \lambda/2$. A similar scaling is observed in free space, i.e., without the microparticle:

$$d + w \approx 1.22\frac{\lambda}{2NA_{obj}}. \tag{4}$$

From relations (3) and (4), it follows that under classical Köhler illumination, isolated objects in the form of nanoholes cannot be resolved by the microsphere beyond the fundamental diffraction limit, since the center-to-center separation remains close to $\lambda/2$. A comparison of relations (3) and (4) indicates that, in the considered configuration, the resolution enhancement provided by the microsphere relative to free space is primarily due to a local increase in the effective objective numerical aperture, as it is noted in Ref. 17. However, NA is bounded by a limiting value of unity; consequently, this effect alone cannot account for the resolution of objects with a center-to-center separation smaller than $\lambda/2$.

For hole diameters exceeding $\lambda/2$, the optical resolution in free space and in the presence of the microsphere becomes nearly identical. In this regime, the objects appear as two touching ring-like intensity distributions and remain distinguishable even at zero edge-to-edge separation. Therefore, a meaningful comparison of resolving power for $w > \lambda/2$ requires objects of a different geometry, such as square apertures.

Under annular illumination, the microsphere enables resolution at separations below $\lambda/2$. We fix the center-to-center distance at $d + w = 0.4\lambda$ and characterize image quality by the contrast $C = I_{middle}/I_{max}$, defined as the ratio of the intensity at the midpoint between adjacent maxima to the maximum image intensity. At $C = 1$, the objects are completely merged, while at $C = 0.8$, they are just resolvable according to the Rayleigh criterion.

Figure 10 shows the dependence of I_{middle}/I_{max} on the inner numerical aperture NA_{inner} for a fixed outer numerical aperture $NA_{outer} = 1$, both for the microsphere [Fig. 10(a)] and for free space [Fig. 10(b)]. The comparison demonstrates that the microsphere strongly enhances partial-coherence effects under annular illumination.

As shown in Fig. 10(a), increasing the nanohole diameter from 0.1 to 0.3λ leads to a monotonic increase in image contrast, improving the resolving capability even for conventional Köhler illumination ($NA_{inner} = 0$).

An experimental study[18] reported an improvement in optical resolution under annular illumination in free space. However, a direct comparison of Figs. 10(a) and 10(b) shows that increasing NA_{inner} leads to a much stronger contrast improvement—and thus, a more pronounced resolution enhancement—in the presence of a microsphere. This enhancement is particularly pronounced for structures with larger diameters.

CONCLUSION

We have presented a theoretical model of microparticle-assisted super-resolution microscopy and applied it to three representative structures commonly encountered in experiments: Blu-ray disks, conducting dimers, and nanodisk arrays. For each geometry, appropriate illumination conditions are considered.

We demonstrate that the presence of high-frequency oscillations in the spatial correlation function of the radiation leads to a substantial enhancement of the resolving power of the microparticle. Such oscillations may originate from different physical mechanisms. These include waves circulating inside the particle that generate secondary illumination of the sample, the specific geometry of the investigated object (e.g., a Blu-ray disk), and the choice of illumination conditions, as demonstrated here for annular illumination. In the latter case, the resolution was shown to depend on the size of the investigated structures, with larger objects exhibiting improved resolvability.

In the absence of rapid oscillations in the correlation function, super-resolution may still arise from a local increase in the effective numerical aperture of the objective. In this regime, the microsphere enables the discrimination of objects with center-to-center separations down to approximately $\lambda/2$.

SUPPLEMENTARY MATERIAL

See the supplementary material for PDFs: Section 1: Source spectrum and geometry for Blu-ray disk reflection calculations; Section 2: Visualization of a dimer array under critical illumination; Section 3: Comparison of Image Fields and Computational Efficiency of the Full and Simple Models; Section 4: Influence of spatial coherence effects for small objects with and without the microsphere; Section 5: Image calculation algorithm based on the Simple Model.

ACKNOWLEDGMENTS

The study was carried out within the framework of the state assignment of the Lomonosov Moscow State University; A. R. B. and B. S. L. thank support from the Foundation for the Development of Theoretical Physics and Mathematics «BASIS» (No. 23-1-1-61).

AUTHOR DECLARATIONS

Conflict of Interest

The authors have no conflicts to disclose.

Author Contributions

A. R. Bekirov: Conceptualization (lead); Investigation (lead); Software (lead); Visualization (lead); Writing – original draft (lead). **N. A. Lystseva:** Formal analysis (equal); Software (equal); Visualization (equal); Writing – review & editing (equal). **N. V. Grednev:** Formal analysis (supporting); Software (supporting);

Visualization (supporting); Writing – review & editing (supporting). **B. S. Luk`yanchuk:** Conceptualization (supporting); Methodology (supporting); Supervision (equal); Writing – review & editing (supporting). **A. A. Fedyanin:** Project administration (equal); Supervision (equal); Writing – review & editing (lead).

DATA AVAILABILITY

The data that support the findings of this study are available from the corresponding author upon reasonable request.

REFERENCES

[1]Z. Wang, W. Guo, L. Li *et al.*, Nat. Commun. **2**, 218 (2011).
[2]S. Yang, J. Yang, R. Ye, Y. Cao, and Y.-H. Ye, Opt. Lett. **50**, 5478–5481 (2025).
[3]G. Wu and M. Hong, Engineering **36**, 102–123 (2024).
[4]A. V. Maslov and V. N. Astratov, Appl. Phys. Lett. **124**, 061105 (2024).
[5]R. Heydarian and C. Simovski, Photonics Nanostruct. Fundam. Appl. **46**, 100950 (2021).
[6]A. R. Bekirov *et al.*, J. Opt. Soc. Am. A **42**, 45–50 (2025).
[7]L. Tsang, J. A. Kong, and K. H. Ding, *Scattering of Electromagnetic Waves: Theories and Applications* (John Wiley & Sons, New York, 2000).
[8]A. R. Bekirov, B. S. Luk'yanchuk, Z. Wang, and A. A. Fedyanin, Opt. Mater. Express **11**, 3646 (2021).
[9]A. Darafsheh *et al.*, Appl. Phys. Lett. **101**, 141128 (2012).
[10]Y. Yan, L. Li, C. Feng *et al.*, ACS Nano **8**, 1809–1816 (2014).
[11]K. W. Allen, N. Farahi, Y. Li *et al.*, Ann. Phys. **527**, 513–522 (2015).
[12]A. R. Bekirov *et al.*, J. Opt. Soc. Am. A **42**, 1627–1634 (2025).
[13]S. Yang *et al.*, J. Phys. Chem. C **123**, 28353–28358 (2019).
[14]A. V. Maslov and V. N. Astratov, Laser Photonics Rev. **20**, e00769 (2025).
[15]L. Mandel and E. Wolf, *Optical Coherence and Quantum Optics* (Cambridge University Press, Cambridge, 1995).
[16]A. Darafsheh, N. I. Limberopoulos, J. S. Derov, D. E. Walker, and V. N. Astratov, Appl. Phys. Lett. **104**, 061117 (2014).
[17]T. Pahl, L. Hüser, S. Hagemeier, and P. Lehmann, Light: Adv. Manuf. **3**, 699–711 (2022).
[18]X. Ma *et al.*, Ultramicroscopy **195**, 74–84 (2018).